Article

Mitochondrial inflexibility ignites tumor immunogenicity in postoperative glioblastoma

Lulu Cheng [1,9], Zezheng Fang[2,9], Junpeng Wang[2,9], Kaiyan Xi[2], Yi Zhang[2], Fan Feng[2], Le Yu [3], Myla Santiago[4], Jingjing Wang[5], Zimei Wu [5], Kang-nan Wang [6], Thomas Daubon [7], Shilei Ni [2] ✉, Yanrong Zhang [1] ✉ & Yulin Zhang [2,8] ✉

Cellular and molecular heterogeneity contributes to the insufficient immunogenicity of glioblastoma multiforme (GBM), a lethal malignancy characterized by post-resection relapse, ultimately leading to limited immune cell infiltration. Here, we report a strategy to boost tumor immunity by activating the endogenous cGAS-STING signaling pathway through in-situ manipulation of the mitochondrial electron transport chain (ETC), thereby augmenting the immune responsiveness of GBM. Under white light irradiation, the synthetic butterfly-shaped photosensitizer B-TTPy disrupts the mitochondrial ETC by producing excessive reactive oxygen species. Synergistically, inhibition of checkpoint kinase 1 amplifies ETC dysfunction, thus enhancing the cytotoxicity of B-TTPy against tumor cells. Our results demonstrate that the in-house-customized Mitochondrial Electron Alteration Nanoparticles in Glioblastoma (MEANING) efficiently activate innate and adaptive immune response by recruiting antigen-presenting cells and cytotoxic T cells to the surgical margin. Moreover, biodegradable hydrogel-medicated surgical cavity treatment with MEANING can reshape the immunosuppressive tumor microenvironment and eliminate residual GBM cells. In sum, our findings establish a local immune activation approach for GBM, to prevent postoperative tumor recurrence and identify ETC blockade as a promising therapeutic strategy for low-immunogenic tumors.

Glioblastoma multiforme (GBM) is a highly aggressive brain tumor traditionally treated with surgical resection followed by radio- and chemotherapy[1–3]. However, the low immunogenicity and suppressed immune environment contribute to the persistence of residual tumor satellites, resulting in frequent postoperative relapse and limited benefit from surgery intervention[4,5]. A critical driver of GBM recurrence is stem cell-like GBM cells, which play a vital role in tumor growth and the unfavorable outcomes of GBM patients[6,7]. The immunosuppressive properties of tumor microenvironment (TME) cause the lack of T cells (especially CD8$^+$ T cells) to generate an adaptive immune

response against residual GBM cells[8]. Mitochondria, as the hub of cellular metabolism, are essential for maintaining the stemness and proliferation of GBM cells and might therefore be a promising object for therapeutic targeting[9,10].

Targeting the mitochondrial electron transport chain (ETC), particularly mitochondrial complexes, emerges as a promising strategy to disrupt the metabolic balance and enhance immune responses against GBM, and mitochondrial dysfunction in tumor cells can also affect the immune microenvironment[11]. By disrupting the ETC, immune cells like T cells and antigen-presenting cells (APCs), can be reactivated[12]. GBM

cells with impaired mitochondrial function are often more susceptible to immune-mediated destruction, and ETC inhibition can enhance the presentation of tumor antigens, making the cancer cells more visible to the immune system[9,13,14].

To explore a multifaceted approach that exploits the immunostimulatory potential of mitochondrial disruption, a mitochondria-targeting drug, B-TTPy, was synthesized. B-TTPy targets the mitochondrial membrane by electrostatic adsorption and amplifies the production of mitochondrial reactive oxygen species (ROS) under the white light irradiation, thereby destroying the mitochondria[15]. GBM cells have evolved various pathways to scavenge ROS, maintaining intracellular redox homeostasis and preserving cellular integrity and functionality. Checkpoint kinase 1 (CHEK1) is a checkpoint gene in the GBM cell cycle, deficiency of CHEK1 was found to be associated with GBM mitochondrial dysfunction and the ROS imbalance within the mitochondria[16]. Interference with CHEK1 synergistically potentiates ETC interference by B-TTPy and enhances cytotoxicity against tumor cells, which could also activate innate immune pathways, particularly through the cGAS-STING signaling axis[17]. Additionally, the engineered cell membrane enabled a synergistic interference attack on tumor cells, subsequently promoting immune surveillance and response in the GBM environment.

The immune-activated Mitochondrial Electron Alteration Nanoparticles in Glioblastoma (MEANING) was developed to achieve combined intervention. Nanoparticles loaded with B-TTPy and si-CHEK1 were delivered via a bio-degradable hydrogel into the postoperative cavity of GBM patients, serving as a localized therapeutic platform. This innovative system not only facilitated targeted drug delivery but also enabled the sustained release of therapeutic agents, ensuring prolonged exposure and efficacy against residual malignancy. Additionally, combining MEANING with white light enhances the spatial and temporal precision of treatment, enabling precise eradication of GBM remnants. This further enhances the recruitment of APCs and cytotoxic T cells to the surgical margin. The orchestrated immune activation could foster a robust antitumor immune response and mitigate the postoperative recurrence[18,19].

In this work, our findings highlight the feasibility of disrupting the ETC to interfere with mitochondrial function, and demonstrate that activation of the cGAS-STING pathway is an effective measure in enhancing immunogenicity in solid tumors, especially in GBM with low mutational burden. Furthermore, by combining metabolic targeting with immune modulation, this approach could prove effective in treating other malignancies with a significant metabolic contribution[20]. Moreover, by using the in-situ hydrogel design, we allow for localized treatment, potentially negating unwanted side effects, which should warrant further evaluation in clinical trials[21].

Results

Synthesis and characterization of mitochondria-targeting B-TTPy

Pervasive utilization of an electron donor-π-acceptor conjugated system in fabricating photosensitizers (PSs) achieves facilitation in the separation between HOMO and LUMO[22,23]. A more pronounced magnitude of separation promotes the intersystem crossing (ISC) process from excited singlet state (S_1) to triplet state (T_n), thereby augmenting ROS generation[24,25]. Concurrently, the increased steric hindrance between the donor, π-bridge, and acceptor moieties may distort the PSs conformation and thus engender a larger dihedral angle between these units, which further magnifies the separation of HOMO and LUMO and reduces the ΔE_{ST}. Herein, a butterfly-shaped PS, designated B-TTPy, was rationally designed and synthesized (Figs. 1a, S1-13). This molecule incorporates two triphenylamine (TPA) units functioning as electron donors, two thiophene units serving as π-bridges, and two pyridinium moieties functioning as electron acceptors and mitochondria-targeting units due to their robust electron-withdrawing

capacity and inherent positivity. These features make B-TTPy a promising agent for targeted mitochondrial delivery and effective tumor eradication.

As illustrated in Fig. 1b, B-TTPy exhibits a broad absorption spectrum extending to 800 nm, making it suitable for white light irradiation. The maximum emission is 770 nm, effectively mitigating tissue autofluorescence interference (Fig. 1c). Notably, with the increased fraction of poor solvent H_2O in DSMO/H_2O system, the fluorescence intensity of B-TTPy is progressively increased (Fig. S14), ensuring the fluorescence emission and ROS generation under physiological environment. ROS generation capability of B-TTPy was detected using 2,2'-(anthracene-9,10-diyldimethanediyl) dipropanedioic acid (ABDA, a commercial $^1O_2$ detection probe) and dihydrorhodamine 123 (DHR123, a specific fluorescent probe for $O_2^{\cdot-}$). B-TTPy showed a 1.5-fold $^1O_2$ generation efficiency compared to commercial PS Rose Bengal (RB) (Figs. 1d, f, S15c, and S15d) and a 5-fold $O_2^{\cdot-}$ generation capability compared to NBS (a typical type I PS) (Figs. 1e, g, S15a and S15b). The intrinsic mechanism of efficient ROS generation of B-TTPy was elucidated by time-dependent density functional theory (TD-DFT) calculations. As depicted in Fig. 1h, significant separation between HOMO-1 (predominantly located on the TPA moiety) and LUMO (primarily situated on thiophene units and pyridinium salts) may be attributed to the highly twisted molecular conformation (26.603° and 26.029° dihedral angle between two thiophene units and between two pyridinium salts, respectively), which was in line with our design rationale. The low ΔE_{S1-T2} value (0.29 eV) further verified the substantial potential for ISC to generate ROS (Fig. 1i). To further confirm the bioaction of the B-TTPy, the mitochondrial-targeting ability was first confirmed as shown in Fig. S16. Moreover, the markedly different IC_{50} values of B-TTPy under light versus dark conditions underscore its ROS-generating capability and associated antiproliferative activity (Fig. S17).

CHEK1 holds potential to be targeted for mitochondria-targeting therapy

The nucleus-to-mitochondria ROS-sensing pathway is critical in cancer cell survival and adaptation, and CHEK1 has been identified as a key nuclear sensor of ROS[26]. In response to mitochondrial ROS, CHEK1 phosphorylates the mitochondrial single-stranded DNA-binding protein 1 (SSBP1), modulating mitochondrial translation[16]. This phosphorylation prevents SSBP1 from localizing to the mitochondria, which in turn reduces mitochondrial ROS levels[27,28]. Bioinformatic analysis of data from TCGA and GTEx databases revealed elevated levels of CHEK1 expression in GBM (Fig. S18). Additionally, high CHEK1 expression levels were correlated with poorer patient prognosis (Fig. S19). To further validate CHEK1 as a synergistic target for B-TTPy in GBM, single-cell transcriptomic data from six GBM samples that from GEO database were acquired and the analysis results showed a higher proportion and level of CHEK1 expression in the proliferating malignant portions of the tumor tissues (Fig. 2a, b, e). CHEK1-expressing cells also exhibited a robust G2M and S phase, as evidenced by cell cycle status examination (Fig. 2c, d). To investigate the characteristics of the CHEK1-high expressing cell clusters, additional bioinformatic analyses were conducted, revealing significant enrichment of stemness-associated genes, particularly SOX2, OLIG2, and NES (Fig. S20a). Furthermore, data from the TCGA database demonstrated a positive correlation between CHEK1 and CD133 expression in GBM (Fig. S20b). Gene Ontology enrichment analysis and Kyoto Encyclopedia of Genes and Genomes pathway analysis indicated that CHEK1 is associated with tumor cell division and DNA repair (Fig. 2f, g). Collectively, these findings highlight the potential of CHEK1 as a therapeutic target for malignant groups in GBM. Therefore, we hypothesized that blocking CHEK1 synergizes with the B-TTPy-produced ROS to disrupt mitochondria, thereby enhancing the therapeutic efficacy.
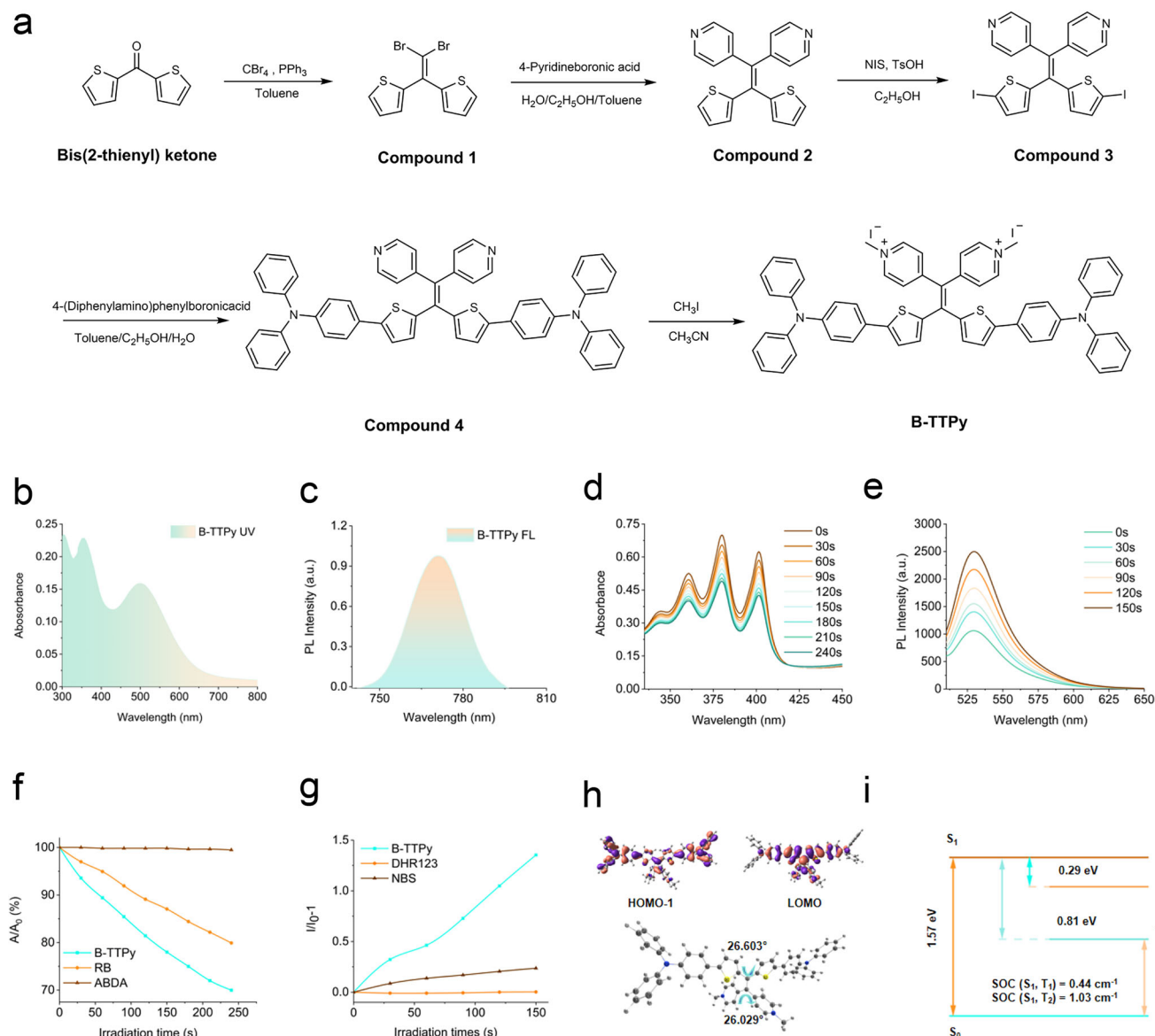
Fig. 1 | Synthesis and characterization of Mito-targeted B-TTPy. a Synthetic route to B-TTPy. **b** Absorption and **c** fluorescence spectra of B-TTPy. **d** Change in absorption spectra of ABDA (50 µM) under white light irradiation in the presence of B-TTPy (10 µM). **e** Change in fluorescence spectra of DHR123 (5 µM) under white light irradiation in the presence of B-TTPy (10 µM) (λ_{ex} = 500 nm). **f** Comparison of $^1O_2$ generation capability of B-TTPy and commercial PS RB. **g** Comparison of O_2^{-} generation efficiency of B-TTPy and type-I PS NBS. **h** HOMO-1/LOMO distributions and optimized structure of B-TTPy. **i** ΔE_{ST} values of B-TTPy by time-dependent density functional theory. Source data are provided as a Source Data file.

Design and characterization of the MEANING-hydrogel delivery system

In this work, effective delivery of si-CHEK1 and B-TTPy to tumor cells was achieved by nanoparticles assembled with the mixture of Poloxamine 704 and RADA16 (PRD) loaded with B-TTPy and si-CHEK1 through electrostatic adsorption (Fig. 3a, b). Subsequently, engineered cell membranes expressing anti-CD133 scFv were wrapped around the surface of the nanoparticles, creating the B-TTPy nanoparticles (BD), co-loading of si-CHEK1 and B-TTPy nanoparticles (CBD), and MEANING (Figs. 3b and S21). Transmission electron microscopy and dynamic light scattering confirmed the uniformity of the nanoparticles, which exhibited a slight increase in size and maintained a negative surface charge after the encapsulation with the engineered cell membranes (Fig. 3c–e). Furthermore, as the ratio of BD to si-CHEK1 increased, the encapsulation efficiency of CBD progressively improved, reaching the maximum when all si-CHEK1 was loaded (Fig. S22). Confocal microscopy results verified the co-loading of B-TTPy and si-CHEK1 within MEANING (Fig. 3f). Particle size stability maintained up to three days in various concentrations of plasma (Fig. 3g). Furthermore, the ROS generation capacity of B-TTPy within MEANING remained unaffected (Fig. S23).

To address the challenges of the post-surgical intracranial environment, characterized by flowing cerebrospinal fluid and voids, a biodegradable Gelatin Methacryloyl (GelMA) hydrogel was utilized to fill the resection cavity. The MEANING-hydrogel showed excellent injectability and gelation properties, facilitating localized, sustained drug release (Figs. 3h, i, S24a)[29,30]. The biodegradable hydrogel could be secured within the cavity through UV curing[31]. The scanning electron microscope exhibited a loose reticular structure of the gel in Figs. 3j and S24b. Dynamic frequency sweep rheological test further revealed that the storage modulus (G′) of the hydrogels consistently exceeded the loss modulus (G″), across the tested frequency range, indicating good mechanical stability (Figs. 3k and S24c). To examine the in vitro degradation of the gel, a dry weight assay was used. When
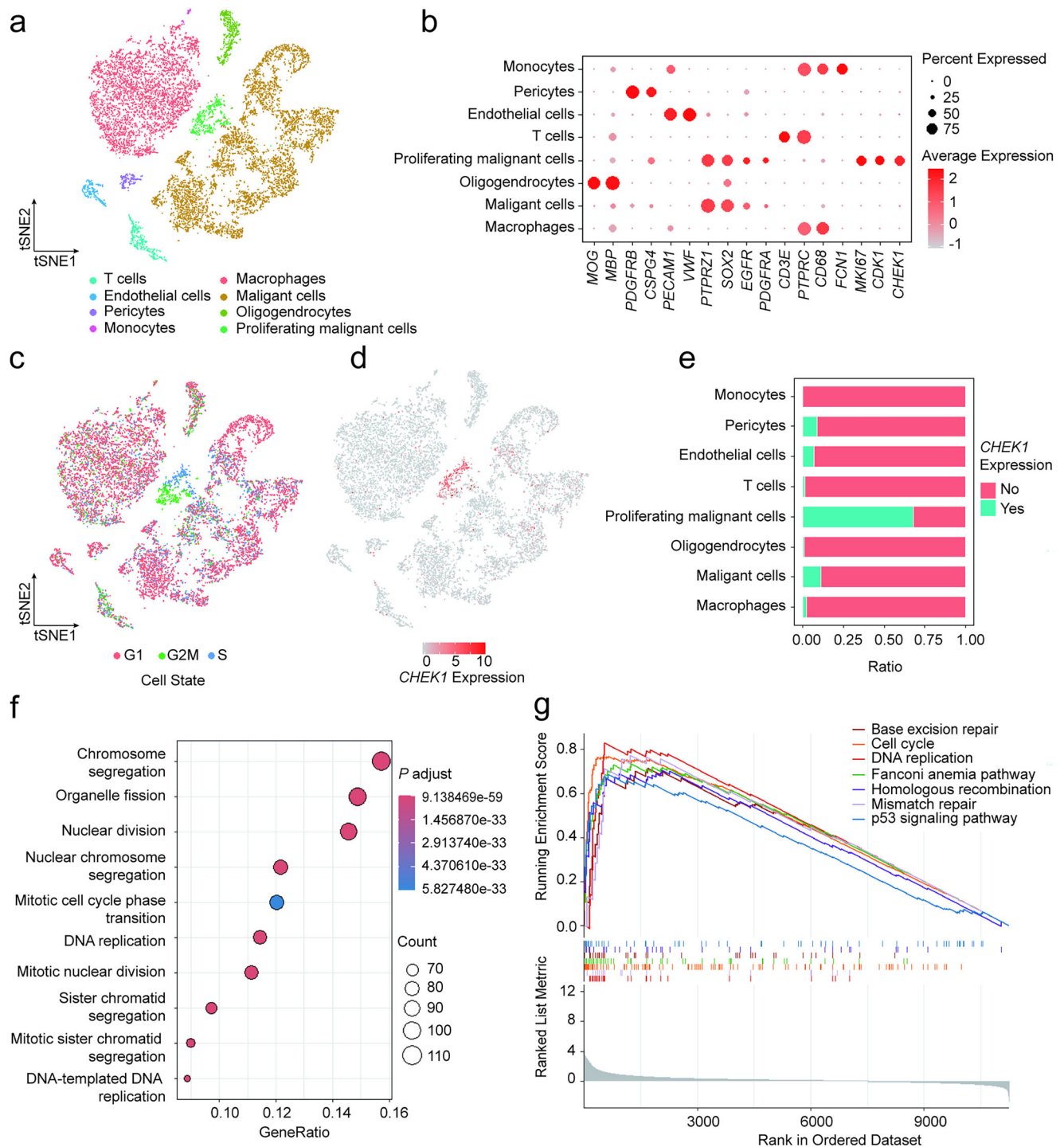
Fig. 2 | *CHEK1* holds potential to be target for mitochondria-targeted therapy.
a t-SNE plot integrating single-cell transcriptomic data from 11,829 cells obtained from 6 GBM samples. Eight distinct cell clusters have been identified and annotated based on their transcriptional profiles. **b** Dot plot displaying the expression of signature genes specific to each of the eight identified cell clusters. The color of the dots represents the relative expression level of the genes, and the size of the dots indicates the proportion of cells expressing the gene within each cluster. **c** t-SNE plot highlighting the distribution of GBM cells according to their cell cycle state. **d** t-SNE plot visualizing the distribution of cells with varying levels of *CHEK1* expression. **e** Bar chart presenting the proportions of cells expressing the *CHEK1* gene within each of the eight cell clusters. **f** Gene Ontology (GO) terms significantly enriched among genes co-expressed with *CHEK1*. **g** Kyoto Encyclopedia of Genes and Genomes (KEGG) pathways significantly enriched in cells expressing the *CHEK1*.

incubated in PBS, the gel degraded continuously over eight days (Fig. 3l). During this period, the MEANING particles encapsulated in the gel exhibited controlled release (Fig. S25). These findings suggest that the biodegradable hydrogels possess a controlled degradation behavior and injectable properties, making them suitable for intracranial biomedical applications.

MEANING induces ROS production and cell death in vitro

In our previous work, we derived primary GBM cells QL01#GBM (Fig S26)[32]. Efficient delivery of the photodynamic drug B-TTPy to QL01#GBM cells was demonstrated through flow cytometry (Fig. 4a). The optimal transfection efficiency was achieved by encapsulating the engineered cell membranes. As the incubation time increased, a greater
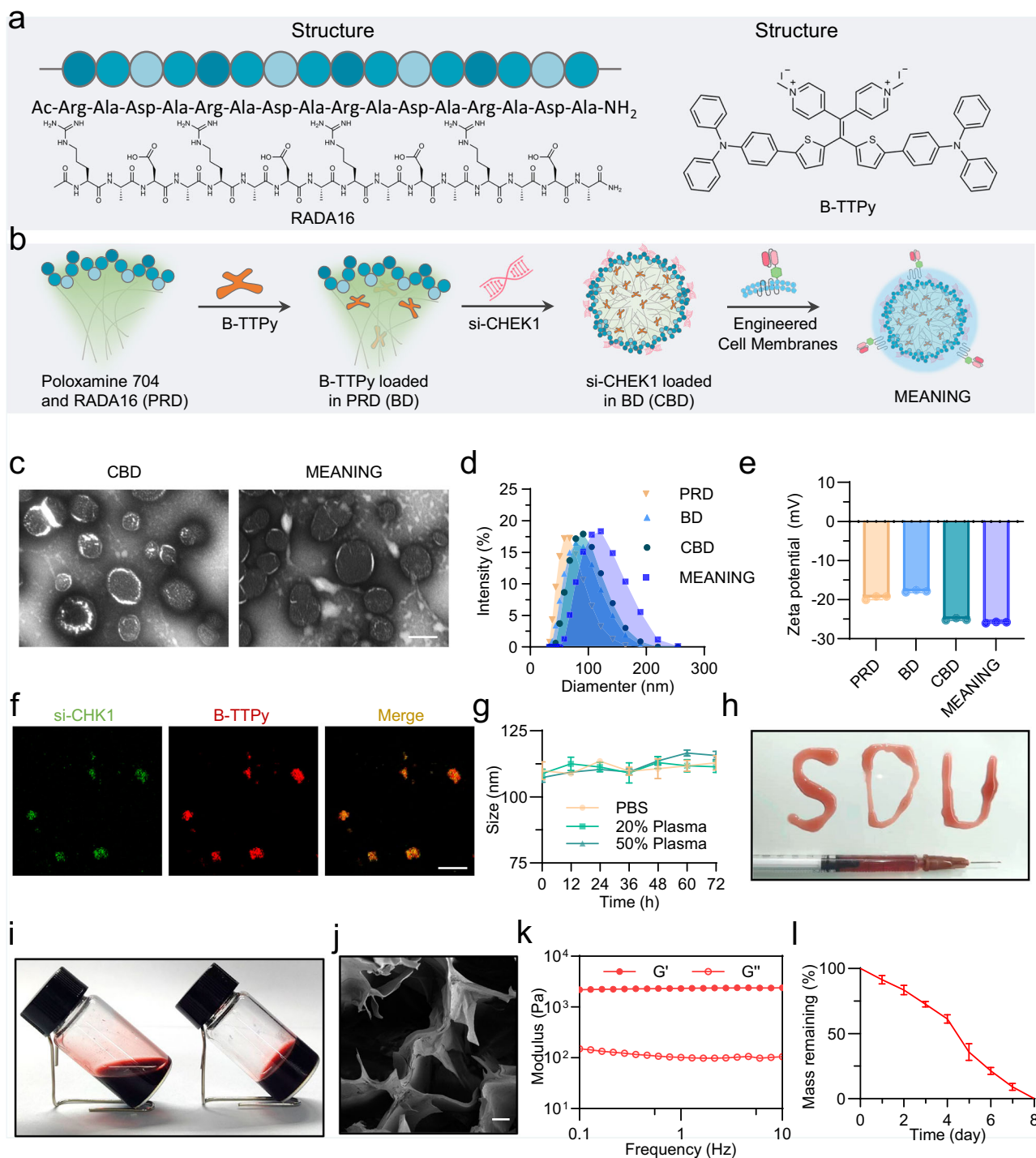
Fig. 3 | Design and characterization of the MEANING-hydrogel delivery system. **a** Molecular formula of the RADA16 and B-TTPy. **b** Schematic illustration of MEANING preparation. **c** TEM image of CBD and MEANING. Scale bar, 100 nm. **d** Size distribution of each nanoparticle. **e** Zeta potential of each nanoparticle. Data are shown as the mean ± S.D. ($n = 3$ independent experiments). **f** Representative fluorescence images of the MEANING, in which si-CHEK1 was labelled with FAM and B-TTPy was red. Scale bar, 200 nm. **g** Stabilities of the MEANING in PBS, PBS with 20% plasma, and PBS with 50% plasma. Data are shown as the mean ± S.D. ($n = 3$ independent experiments). **h** The MEANING-hydrogel was freely molded into diverse geometric shapes using a syringe. **i** Representative photographs of MEANING-hydrogel before and after gel formation. **j** SEM image of the MEANING-hydrogel. Scale bar, 50 μm. **k** Rheology traces of the MEANING-hydrogel. **l** The degradation of the hydrogels in vitro. Data are shown as the means ± S.D. ($n = 3$ independent experiments). Source data are provided as a Source Data file.

amount of B-TTPy accumulated within the tumor cells was observed (Fig. 4b). Additionally, the investigation into intracellular CHEK1 levels revealed that treatment with CBD and MEANING significantly inhibited CHEK1 expression (Figs. 4c and S27). These findings strongly support the targeting delivery of MEANING to QL01#GBM cells. Subsequently, to investigate cellular effect of MEANING, the production of ROS in the cells

following white light irradiation was evaluated. Notably, MEANING exhibited the highest efficiency in delivering B-TTPy into the cells, consequently leading to the highest ROS concentration and increased level of NOX post-irradiation (Figs. 4d, e, S28). Cell viability was then examined, and in alignment with the above results, the group treated with MEANING demonstrated a substantial decrease in cell viability under
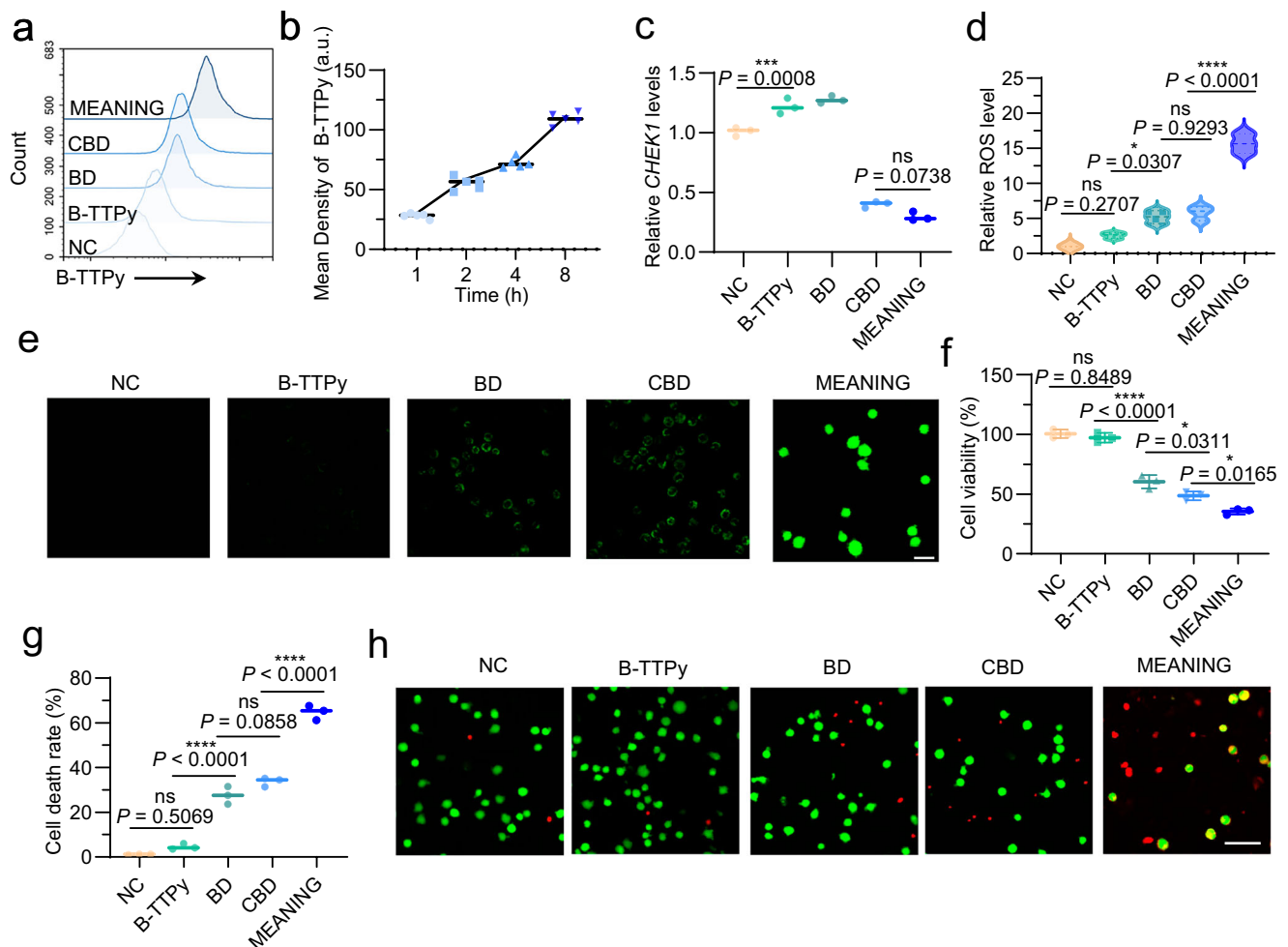
Fig. 4 | MEANING induces ROS production and cell death in vitro. a Cellular uptake of B-TTPy loaded in different nanoformulation by QL01#GBM cells was analyzed by flow cytometry. **b** Statistical analysis of the fluorescence intensity of intracellular B-TTPy at different time points. Data are shown as the mean ± S.D. ($n = 5$ independent experiments). **c** CHEK1 expression levels in QL01#GBM cells exposed to different treatments. Data are shown as the mean ± S.D. ($n = 3$ independent experiments). Data are analyzed with one-way ANOVA. **d** Statistical analysis of ROS level of QL01#GBM cells after treatment with different nanomedicines. Data are shown as the mean ± S.D. ($n = 3$ independent experiments) (exact P value: $P = 7.10603E-07$). Data are analyzed with one-way ANOVA. **e** Confocal laser scanning microscopy imaging of the intracellular ROS levels (green fluorescence from dichlorofluorescein (DCF) in the reaction between DCFH-DA and ROS of QL01#GBM cells following various treatments. Scale bar, 20 μm. **f** Cell viability was determined by CCK8 assays after treatment with each nanoformulation. Data are shown as the mean ± S.D. ($n = 3$ independent experiments) (exact P value: $P = 4.10338E-06$). Data are analyzed with one-way ANOVA. **g** Quantitative analysis and **h** Confocal live/dead cell fluorescence imaging of QL01#GBM cells treated with each formulation. Green from Calcein indicates live cells, red from PI denotes dead cells, and the yellow color results from co-staining of Calcein and PI. Data are shown as the mean ± S.D. ($n = 3$ independent experiments) (exact P value: B-TTPy vs. BD $P = 4.46967E-06$; CBD vs. MEANING $P = 2.73496E-07$). Data are analyzed with one-way ANOVA. *$P < 0.05$, **$P < 0.01$, ***$P < 0.001$, ****$P < 0.0001$. Source data are provided as a Source Data file.

white light irradiation conditions (Fig. 4f). Cell live/dead staining further revealed a highest cell death rate in the MEANING group (Fig. 4g, h). In addition, another patient-derived primary tumor cells with lower CD133 expression levels were harvested to investigate the efficacy of the MEANING system in CD133-high versus CD133-low cells, and the results showed superior efficiency of MEANING in QL01#GBM compared to the CD133-low tumor cells (Fig. S29). These results affirm the efficacy of MEANING in generating ROS and inducing GBM cell demise. Similar treatment efficacy was observed in the CT-2A and GL261 cell lines (Figs. S30 and S31). Additionally, MEANING showed no significant cytotoxicity in the normal human astrocyte (NHA) cell line, indicating its relative safety (Fig. S32).

MEANING caused mitochondrial damage and induced immunogenic cell death in malignant GBM cells
Initial studies confirmed that B-TTPy targets mitochondria, generating ROS under white light irradiation. We proposed a hypothesis that

MEANING interferes with tumor cell ETCs by disrupting mitochondrial function, subsequently inducing cell death (Fig. 5a). Electron microscopy revealed significant swelling and deformation of mitochondria in MEANING-treated cells compared to controls, suggesting effective disruption of mitochondrial integrity (Fig. 5b). Further examinations assessed mitochondrial membrane potential by the TMRE probe (Fig. 5c, d). Findings indicated a loss of normal mitochondrial membrane potential in MEANING-treated cells upon white light irradiation, in contrast to the significant negative potential maintained in untreated cells. The disruption was also manifested as an increase in mitochondrial permeability, especially in MEANING treatment (Figs. 5e, f, S33). Additionally, following MEANING treatment, an increased localization of SSBP1 to the mitochondria was observed, which correlated with the highest levels of ROS in the cells (Figs. 5g and S34). Besides, the levels of ATP and HMGB1 release, markers of immunogenic death of tumor cells, were also greatly increased after nanoparticles were combined with white light

irradiation, and MEANING resulted in the maximum concentration of ATP and HMGB1 release (Fig. 5h, i). The increased expression levels of cGAS, STING and pIRF3 following MEANING treatment indicated the immune activation (Fig. S35), and the downstream cytokines CXCL10 and IFN-β were also upregulated (Figs. 5j, k and S36). These results collectively highlight MEANING's dual functionality: targeting mitochondria to disrupt their structure and perturbing the ETC, thus inducing the immunogenic death of tumor cells.

Evaluation of postoperative in vivo antitumor efficacy of MEANING-hydrogel

The MEANING was mixed with hydrogel solution to create the MEANING-hydrogel to apply the clinical requirement. To evaluate the clinical potential of MEANING-hydrogel, a GBM model was established using 6-week C57 mice. The model involved the orthotopic injection of GL261 Luciferase$^+$ cells into the brain to develop an in-situ tumor. Ten days post-injection, the tumors were surgically resected, and the resultant cavities were filled with the MEANING-hydrogel (Fig. 6a, b). Post-surgical examination of the mouse brain sections revealed the presence of residual tumor cells (Fig. 6c). Moreover, recurrent tumors in mice models displayed scattered CD133-expressing tumor cells, suggesting the persistence of highly tumorigenic cells (Fig. S37). The progression and response to treatment were monitored through bioluminescence imaging, which indicated superior tumor suppression in mice treated with MEANING-hydrogel compared to controls (Fig. 6d, e). Mice in G1 were treated with PBS after tumor resection and demonstrated a median survival of only 28 days. In contrast, the MEANING-hydrogel treated group showed not only a significant reduction in tumor recurrence but also an extended survival rate. 40% tumor-bearing mice achieved long-term survival after MEANING-hydrogel treatment (Fig. 6f). The blood chemistry analysis of mice after various treatments showed no obvious systemic toxicity (Fig. 6g). Furthermore, Ki67 staining of tumor tissue sections also showed similar efficacy to the above results, with mice in G5 showing lower levels of Ki-67 positive cells (Fig. 6h, i). These findings demonstrated the effectiveness of MEANING as a promising therapeutic strategy for inhibiting the postoperative recurrence of GBM and enhancing survival outcomes in a clinical setting.

In vivo antitumor mechanisms of postoperative injection of MEANING-hydrogel

To elucidate the mechanism by which long-term MEANING-hydrogel treatment impedes the recurrence of GBM in vivo, mice were euthanized 21 days post-surgery, and tumor tissues were harvested for analysis (Fig. 7a). Immune cell infiltration in tumor tissue revealed by flow cytometry indicated enhanced immune response. Particularly noting an increase in CD3$^+$CD4$^+$ (31.61%) and CD3$^+$CD8$^+$ (31.12%) T cells in G5 mice, which were 3.844 and 3.534-fold higher than those in control group (8.223% and 8.807%), respectively (Figs. 7b, c S38 and S39a). Furthermore, regulatory T cells (Tregs), which contribute to immune suppression, were significantly reduced in MEANING-hydrogel-treated mice, decreasing to 18.35% compared to 37.12% in G1 (Figs. 7d and S39b). The OT1-tetramer system was used to assess tumor-specific T-cell infiltration following different treatments. The results showed that 261-OVA tumor-bearing mice treated with MEANING-hydrogel exhibited the highest levels of OVA-specific T-cells, providing evidence of enhanced tumor-specific T-cell accumulation in the treated mice (Figs. 7e and S39c).

Since MEANING could induce tumor cells to undergo immunogenic cell death, leading to the exposure of tumor antigens from dying cells. As the APCs in tumor tissues, the roles of tumor-associated macrophages (TAMs) and dendritic cells (DCs) within the tumor immune microenvironment were also investigated. A significant shift was observed in the polarization of macrophages, with an increase in M1-polarized macrophages (Figs. 7f, g, S40a and S40b), which are associated with tumoricidal activity. Meanwhile, a decrease in the M2 phenotype, which tends to be immunosuppressive, was also observed (Figs. 7h, i, S40c, and S40d). This change was quantified as a notable increase in the M1/M2 ratio, which was 9.331-fold higher than that in the G1 group (Fig. S40e). Additionally, dramatic upregulation of MHC II on DCs was observed in the G5 mice (Figs. 7j and S41). Cytokine analysis showed elevated levels of IFN-γ, TNF-α, and IL-12, and a decrease in TGF-β, indicating a robust anti-tumor immune response induced by MEANING-hydrogel treatment (Fig. 7k, l).

To determine whether the immune response impacts the outcome of MEANING-hydrogel treatment, we treated nude mice bearing GL261 tumors with PBS or MEANING-hydrogel. MEANING-hydrogel therapy in C57 mice led to much greater tumor control compared with PBS (Fig. 6d–f). In the nude mouse model, MEANING-hydrogel treatment inhibited tumor progression to a limited extent, but all treated mice ultimately succumbed to tumor recurrence under the same dose of MEANING-hydrogel (Fig. S42). These findings demonstrated that the MEANING-hydrogel, through its localized and sustained release of mitochondria-targeting nanoparticles, disrupted ETC, induced tumor cells immunogenic death, and ultimately enhanced anti-tumor immunity, ameliorated the immunosuppressive tumor microenvironment, and effectively eradicated GBM cells.

Discussion

Clinically, the management of GBM remains one of the most formidable challenges in neuro-oncology, largely due to the aggressive nature, low immunogenicity, and the persistence of residual tumor cells post-surgery[33,34]. Our study introduced an innovative approach to addressing these challenges by leveraging the disruption of the mitochondrial ETC to enhance the immunogenicity of GBM, thus exploring new avenues for therapeutic intervention. Interventions to enhance the immunogenicity of tumor cells are key to activating the immune system and represents an effective strategy for achieving immunotherapy in tumors with low mutational burden[34,35].

Mitochondria, often referred to as the cellular powerhouses, are central to the metabolic adaptations that sustain the stemness and proliferation of malignancy[15,36]. By disrupting the ETC through the combination of the synthesized photosensitizer and blockage of CHEK1, we aimed to perturb the metabolic equilibrium that tumor cells rely on for survival. Our results confirmed that this strategy effectively generated intolerable levels of ROS within the mitochondria, leading to significant mitochondrial damage and subsequent tumor cell death. This finding is particularly important given the role of mitochondria in maintaining the stem-like characteristics of the malignancy, which are often implicated in GBM recurrence and resistance to conventional therapies.

One of the most compelling aspects of our approach is the ability of the mitochondrial disruption to induce ICD, a process that not only eliminates tumor cells but also enhances the visibility of residual tumor cells to the immune system[37]. Our study demonstrated that the ROS generated by B-TTPy under white light irradiation triggered the release of ATP and HMGB1, hallmarks of ICD, and activated the cGAS-STING signaling pathway. The activation of this pathway is crucial for initiating a robust innate immune response, particularly in tumors with low mutational burdens like GBM, which typically evade immune detection[38,39]. The observed increase in cGAS and STING expression following treatment with the MEANING nanoparticles underscores the potential of this approach to not only kill tumor cells directly but also to prime the immune system for a sustained anti-tumor response.

The clinical translation of our findings was further enhanced by the development of the MEANING-hydrogel delivery system, which was designed to address the specific challenges of the post-surgical intracranial environment. The GelMA hydrogel provided a platform for the localized and sustained release of the MEANING nanoparticles,
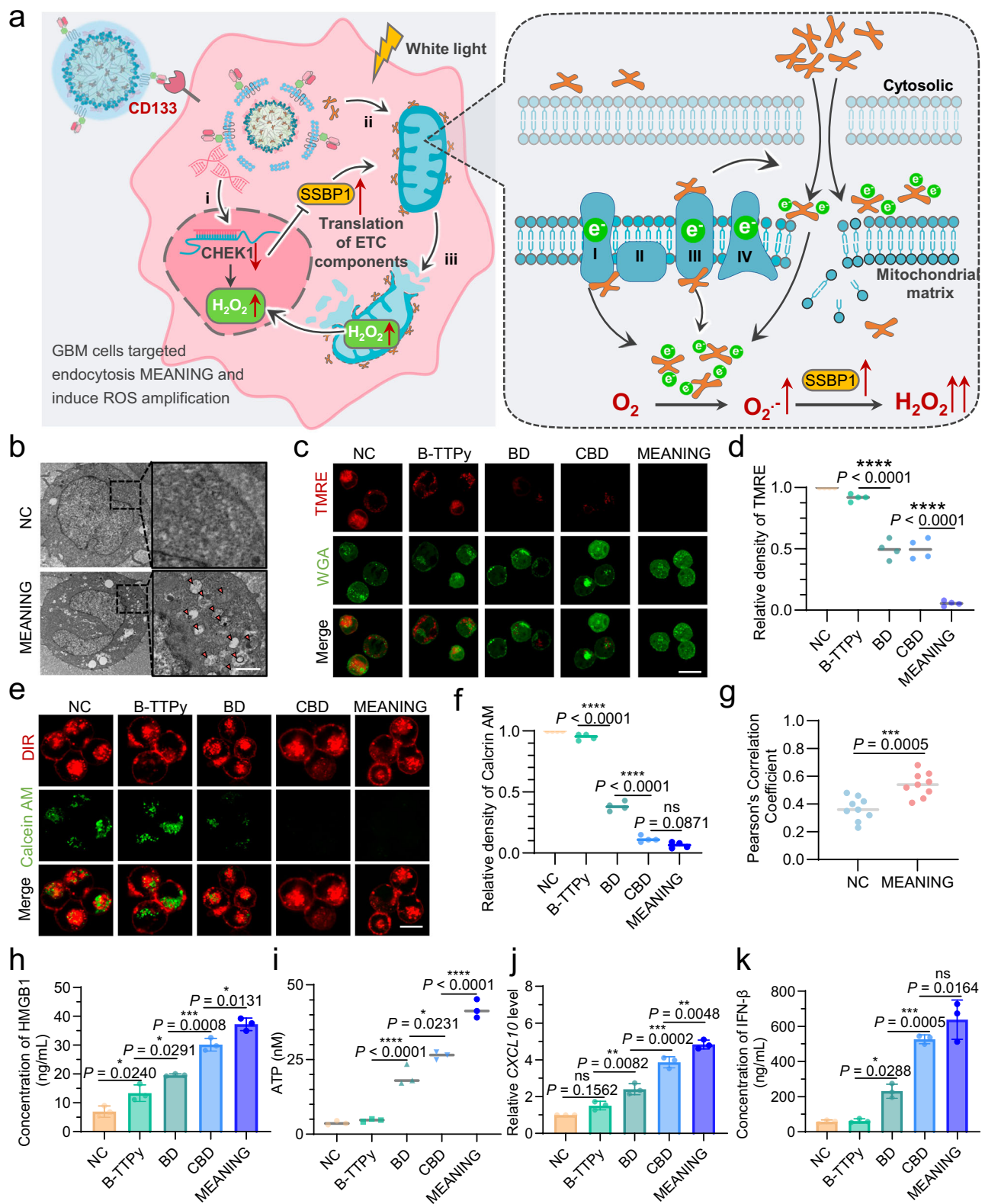
ensuring prolonged exposure of residual tumor cells to the therapeutic agents. This approach effectively minimized the risk of GBM recurrence, as evidenced by the extended survival and reduced tumor burden in vivo models. The MEANING-hydrogel ensured sustained release of MEANING within the resection cavity, even during the continuous cerebrospinal fluid circulation, which is a significant advancement, providing a practical solution to one of the key obstacles in post-surgical GBM therapy.

In addition to directly targeting CD133^{+}GBM cells, our study highlights the broader immunomodulatory effects of the MEANING-hydrogel. We observed a significant shift in the tumor immune microenvironment, characterized by increased infiltration of CD8^{+} T cells and a reprogramming of TAMs towards an M1-like phenotype. This polarization towards a tumoricidal state is critical for overcoming the immunosuppressive barriers typically present in GBM. Our findings also suggested that the combination of mitochondrial targeting

Fig. 5 | MEANING caused mitochondrial damage and induced immunogenic death in malignant GBM cells. a Schematic illustration of the mechanism that MEANING induce mitochondria damage. i) si-RNA silence expression of CHEK1. ii) B-TTPy molecules locate in mitochondria and produce ROS upon the light irritation. iii) mitochondria contents release and induce GBM cell immunogenicity death. **b** TEM image of normal mitochondria (above) and damaged mitochondria (below). Scale bar, 1 μm. **c** Confocal laser scanning microscopy imaging and **d** quantitative analysis of red fluorescence intensity from tetramethylrhodamine, ethyl ester (TMRE) in QL01#GBM cells. Scale bar, 15 μm. Data are shown as the mean ± S.D. ($n = 4$ independent experiments) (exact P value: B-TTPy vs. BD $P = 1.00742E-07$; CBD vs. MEANING $P = 5.00642E-08$). Data are analyzed with one-way ANOVA. **e** Confocal laser scanning microscopy imaging and **f** quantitative analysis of green fluorescence intensity from calcein acetoxymethyl ester (Calcein AM) in QL01#GBM cells. Scale bar, 10 μm. Data are shown as the mean ± S.D. ($n = 4$ independent experiments) (exact P value: BD vs. CBD $P = 1.89336E-09$). Data are analyzed with one-way ANOVA. **g** Pearson's correlation coefficient of SSBP1 with Mitotracker Green. Data are shown as the mean ± S.D. ($n = 9$ images from three independent experiments). Data are analyzed with two-tailed, unpaired Student's t-test. **h** HMGB1 release from QL01#GBM cells after different treatments. Data are shown as the mean ± S.D. ($n = 3$ independent experiments). Data are analyzed with one-way ANOVA. **i** The levels of ATP release after different treatments. Data are shown as the mean ± S.D. ($n = 3$ independent experiments) (exact P value: B-TTPy vs. BD $P = 6.31757E-05$; CBD vs. MEANING $P = 4.21364E-05$). Data are analyzed with one-way ANOVA. *$P < 0.05$, **$P < 0.01$, ***$P < 0.001$, ****$P < 0.0001$. **j** *CXCL10* expression level in QL01#GBM cells after different treatments. Data are shown as the mean ± S.D. ($n = 3$ independent experiments). Data are analyzed with one-way ANOVA. **k** IFN-β release from QL01#GBM cells after different treatments. Data are shown as the mean ± S.D. ($n = 3$ independent experiments). Data are analyzed with one-way ANOVA. Source data are provided as a Source Data file.

with immune modulation could represent a synergistic strategy for enhancing anti-tumor immunity.

While our study provides a promising foundation for an innovative GBM therapy, several aspects warrant further investigation. The long-term safety and efficacy of the MEANING-hydrogel in clinical settings must be rigorously evaluated, particularly with respect to potential off-target effects and the durability of the immune response. Moreover, the view of targeting mitochondrial function to enhance tumor immunogenicity could have broader implications for other low-immunogenicity tumors beyond GBM. Future studies could explore the applicability of this approach to other malignancies, potentially in combination with existing immunotherapies to further amplify therapeutic outcomes.

Collectively, in this work, our experiments demonstrate that disrupting the mitochondrial ETC represents a viable strategy for combating the inherent challenges of GBM, particularly in terms of tumor recurrence and immune evasion. The combination of mitochondrial-targeted disruption with localized immune modulation presents a powerful approach to enhancing the immunogenicity of GBM, paving the way for more effective post-surgical therapies. As this approach progresses towards clinical application, it holds the promise of improving outcomes not only for GBM patients but also for those with other intractable cancers.

Methods

Ethics statement

All animal experiments were approved by the Research Ethics Committee of Shandong University and the Ethics Committee of Qilu Hospital (Shandong, China). Ethical constraints included the following: tumor volume was strictly limited to ≤ 10% of the animal's body weight, and body weight loss was maintained below 20% throughout the study period. No animals exceeded predefined tumor burden thresholds.

Materials

All reagents and solvents (analytical grade) were used as received from commercial sources unless otherwise indicated. Solvents were purified by standard procedures. Fetal bovine serum (FBS), neurobasal medium, B-27 serum-free supplement, epidermal growth factor (EGF) and basic fibroblast growth factor (bFGF) were purchased from Gibco. Dulbecco's modified Eagle's medium (DMEM), penicillin, trypsin-EDTA, and RIPA lysis buffer were obtained from Thermo Fisher Scientific, Inc. Cell Counting Kit-8, cell culture freezing medium and enhanced chemiluminescence reagent were purchased from New Cell & Molecular Biotech Co. Ltd. A live/dead viability/cytotoxicity kit, DMSO, propidium iodide (PI), PKH26 membrane dye, thrombopoietin (TPO) and nitrosoglutathione (GSNO) were purchased from Sigma–Aldrich, Inc. Lipofectamine RNAiMAX, Lipofectamine 3000 and wheat germ agglutinin conjugated to Alexa Fluor™ 488 were purchased from Invitrogen. Mito-Tracker Green, DAPI, PMSF protease inhibitor, the

BCA protein assay kit, the ROS Content Assay Kit, the Mitochondrial Permeability Transition Pore Assay Kit, the Mitochondrial Membrane Potential Assay Kit and antibody dilution buffer were obtained from Beyotime Biotech., Inc. The horseradish peroxidase-conjugated secondary antibody was purchased from ZSGB-BIO. Phosphate-buffered saline (PBS) and the ROS Content Assay Kit were purchased from Beijing Solarbio Science & Technology Co., Ltd. ELISA kits for mouse TGF-β, IL-12, TNF-α and IFN-γ were purchased from Lianke Bio. The antibodies used in this study were summarized as follows (company, Catalog number, Clone name, dilutions): CD3-PerCP-Cy5.5 (BioLegend, Catalog number: 100218; Clone name: 17A2; 1:20 dilution); CD4-PE (BioLegend, Catalog number: 100408; Clone name: GK1.5; 1:100 dilution); CD8-FITC (BioLegend, Catalog number: 100706; Clone name: 53-6.7; 1:50 dilution); CD80-PE (BioLegend, Catalog number: 104708; Clone name: 16-10A1; 1:40 dilution); CD206-APC (BioLegend, Catalog number:141708; Clone name: C068C2; 1:40 dilution); F4/80-FITC (BioLegend, Catalog number:123108; Clone name: BM8; 1:200 dilution); β-Tubulin (Cell Signaling Technology, Catalog number: 2146; 1:1000 dilution); STING (Cell Signaling Technology, Catalog number: 50494 T; D1V5L; 1:1000 dilution); GAPDH (Cell Signaling Technology, Catalog number: 2118; 14C10; 1:1000 dilution); cGAS(Cell Signaling Technology, Catalog number: 79978; E5V3W; 1:1000 dilution); MHC II-APC (BioLegend, Catalog number:116417; Clone name: AF6-120.1; 1:30 dilution); iNOS-PE (BioLegend, Catalog number: 696805; Clone name: W16030C; 1:160 dilution); Arg1-PE(BioLegend, Catalog number: 165803; Clone name: W210471; 1:160 dilution); CD11c-FITC(BioLegend, Catalog number:117305; Clone name: N418; 1:200 dilution); T-Select H-2Kb OVA Tetramer-SIINFEKL-APC(MEDICAL & BIOLOGICAL LABORATORIES, Catalog number: TS-5001-2C; 1:10 dilution); pIRF3 (Cell Signaling Technology, Catalog number: 4947; 4D4G; 1:1000 dilution). The sequences of all the DNA, primers and CpG sites can be found in Supplementary Tables 1 and 2.

Cell culture and animal studies

The mouse glioma cell line GL261 and CT-2A were acquired from the Cell Bank of the Chinese Academy of Sciences (Shanghai, China), while primary human GBM surgically propagated QL01#GBM cells were obtained from the Department of Neurosurgery at Qilu Hospital, Shandong University. GL261 and CT-2A cells were cultured in DMEM supplemented with 10% FBS in a humidified incubator with 5% CO_2 at 37 °C. QL01#GBM cells were cultured in neurobasal medium supplemented with 2% B-27 Serum-Free Supplement, 20 ng/mL EGF, and 10 ng/mL bFGF in a humidified incubator with 5% CO_2 at 37 °C. To assess luminescence intensity, fluorescein-labeled GL261 cells were identified using an in vivo imaging system. All cell lines were authenticated by short tandem repeat (STR) analysis and were tested using the BeyoDirect™ Mycoplasma qPCR Detection Kit (Beyotime, Catalog number: C0303S) for routine screening of mycoplasma contamination.
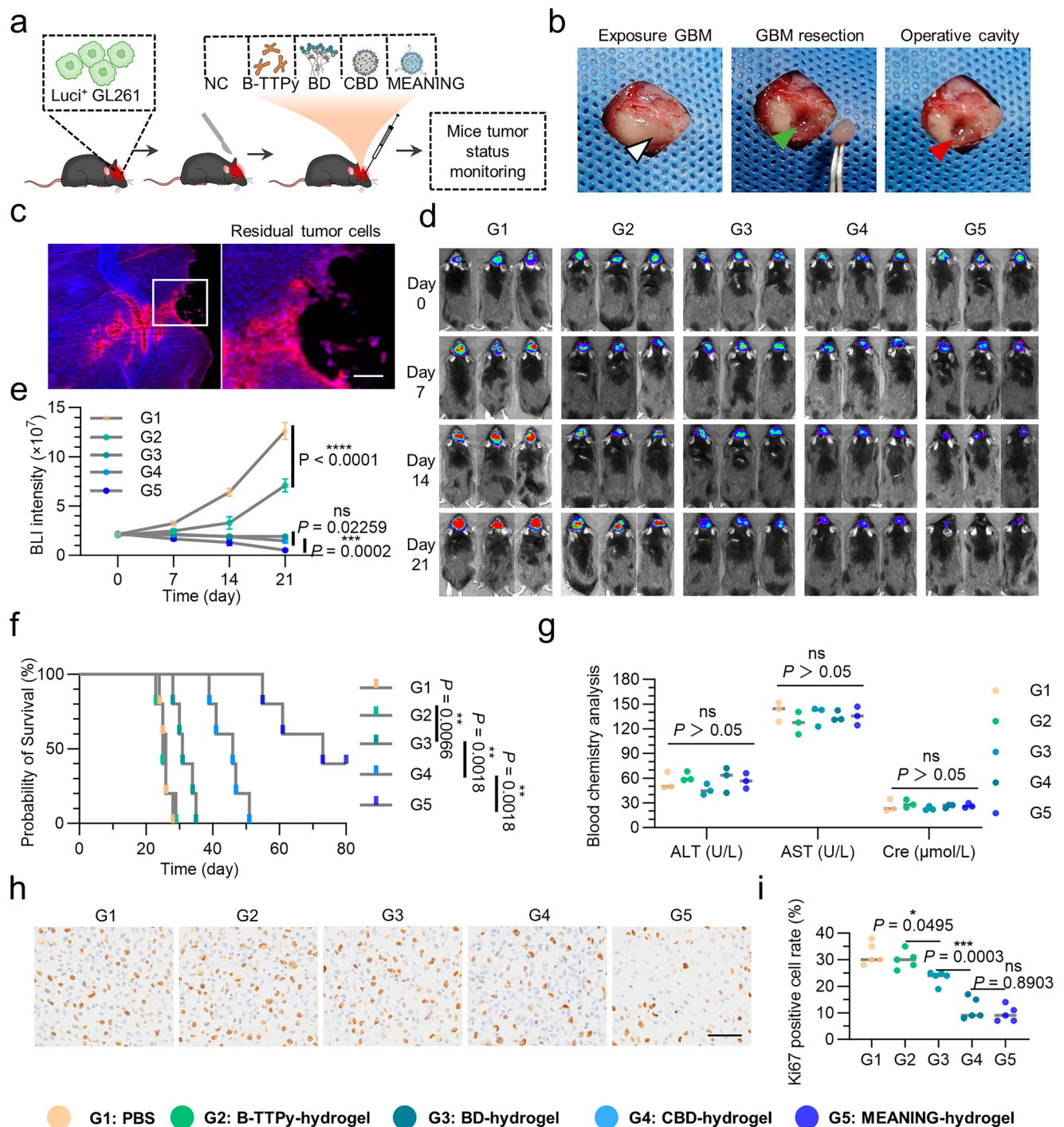
Fig. 6 | Evaluation of postoperative in vivo antitumor efficacy of MEANING-hydrogel. a Schematic illustration of the experimental design. **b** Photograph of the postoperative modeling in GL261 bearing mouse. **c** Immunofluorescence images showing residual tumor cells around the surgical cavity. Blue: DAPI; red: RFP (GL261-RFP cell line). Scale bar, 200 μm. **d** Representative IVIS spectrum images and **e** quantification of the bioluminescence signal intensity of the mice after each treatment. Data are shown as the mean ± S.D. (n = 5 mice). Statistical significance was calculated using two-way ANOVA. **f** Kaplan-Meier survival curves of each group. Data are shown in means ± S.D. (n = 5 mice). Data were analyzed with the log-rank (Mantel-Cox) test. **g** Blood chemistry analysis in mice after different treatments.

Data are shown as the mean ± S.D. (n = 3 independent experiments). Data are analyzed with one-way ANOVA. **h** Ki67 staining of the tumor-bearing mice after different treatments. Scale bar, 50 μm. **i** Quantitative analysis of Ki67 positive level. Data are shown as the mean ± S.D. (n = 5 images from three independent experiments). Data are analyzed with one-way ANOVA. G1, Group 1 treated with PBS after tumor resection (control); G2, Group 2 treated with B-TTPy-hydrogel after tumor resection; G3, Group 3 treated with BD-hydrogel after tumor resection; G4, Group 4 treated with CBD-hydrogel after tumor resection; and G5, Group 5 treated with MEANING-hydrogel after tumor resection. *$P < 0.05$, **$P < 0.01$, ***$P < 0.001$, ****$P < 0.0001$. Source data are provided as a Source Data file.

For in vivo studies, C57BL/6 mice (male, 6 weeks) and OT-1 mice were ordered from Beijing Vital River Laboratory Animal Technology Co., Ltd. Nude mice (male 4 weeks) and H11-OT1 mice (male 6 weeks) were purchased from GemPharmatech Co., Ltd. (Nanning, China). Mice were housed in a temperature-controlled environment (24 ± 1 °C, 50 ± 5% humidity) with a 12 h/12 h light-dark cycle, and provided free access to standard diet and sterile water. Sex-based differences were not investigated as a variable in the experimental design.
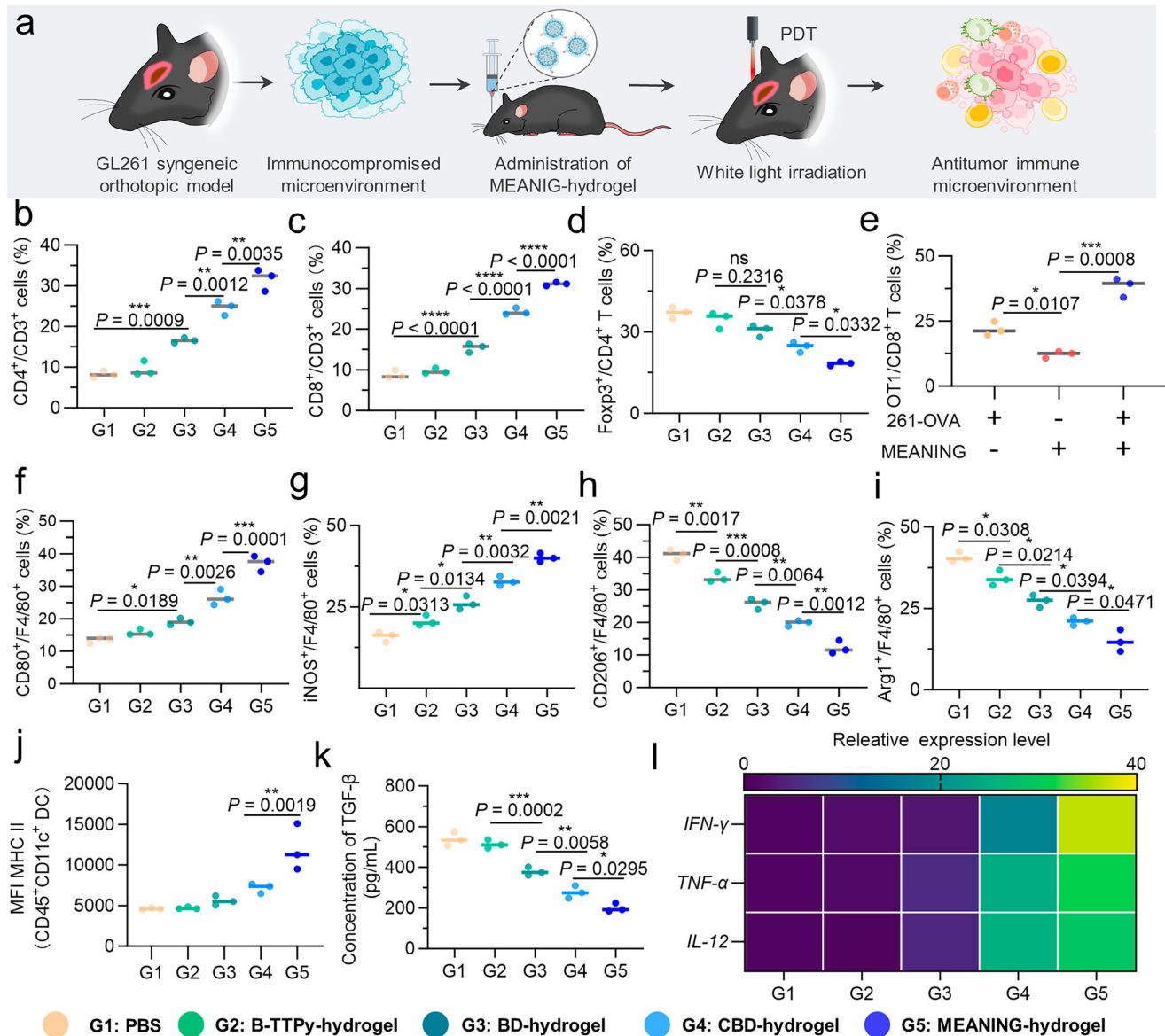
Fig. 7 | In vivo antitumor mechanism of postoperative injection of MEANING-hydrogel. a Schematic illustration of tumor cavity injection of the MEANING-hydrogel combined with white light irradiation to realize an antitumor response. **b** Quantitative analysis of CD3⁺CD4⁺ T cells. Data are shown as the mean ± S.D. ($n = 3$ independent experiments). Data are analyzed with one-way ANOVA. **c** Quantitative analysis of CD3⁺CD8⁺ T cells. Data are shown as the mean ± S.D. ($n = 3$ independent experiments) (exact P value: G1 vs. G3 $P = 1.574E\text{-}05$; G3 vs. G4 $P = 1.13764E\text{-}06$; G4 vs. G5 $P = 1.26878E\text{-}05$). Data are analyzed with one-way ANOVA. **d** Quantitative analysis of Foxp3⁺CD4⁺ T cells. Data are shown as the mean ± S.D. ($n = 3$ independent experiments). Data are analyzed with one-way ANOVA. **e** Quantitative analysis of OVA-specific CD8⁺ T cells. Data are shown as the mean ± S.D. ($n = 3$ independent experiments). Data are analyzed with one-way ANOVA. **f** Quantitative analysis of F4/80⁺CD80⁺ cells. Data are shown as the mean ± S.D. ($n = 3$ independent experiments). Data are analyzed with one-way ANOVA. **g** Quantitative analysis of F4/80⁺iNOS⁺ cells. Data are shown as the mean ± S.D. ($n = 3$ independent experiments).

Data are analyzed with one-way ANOVA. **h** Quantitative analysis of F4/80⁺CD206⁺ cells. Data are shown as the mean ± S.D. ($n = 3$ independent experiments). Data are analyzed with one-way ANOVA. **i** Quantitative analysis of F4/80⁺Arg⁺ cells. Data are shown as the mean ± S.D. ($n = 3$ independent experiments). Data are analyzed with one-way ANOVA. **j** Quantitative analysis showing MHCII expression in intratumoral CD11c⁺ DCs. Data are shown as the mean ± S.D. ($n = 3$ independent experiments). Data are analyzed with one-way ANOVA. **k** Statistical analysis of TGF-β level in GBM tissues after different treatment. Data are shown as the mean ± S.D. ($n = 3$ independent experiments). Data are analyzed with one-way ANOVA. **l** Heatmap of *IFN-γ*, *TNF-α* and *IL-12*, expression profiles in brain tumor tissues. G1, Group 1 treated with PBS after tumor resection (control); G2, Group 2 treated with B-TTPy-hydrogel after tumor resection; G3, Group 3 treated with BD-hydrogel after tumor resection; G4, Group 4 treated with CBD-hydrogel after tumor resection; and G5, Group 5 treated with MEANING-hydrogel after tumor resection. *$P < 0.05$, **$P < 0.01$, ***$P < 0.001$, ****$P < 0.0001$. Source data are provided as a Source Data file.

Mitochondria staining

Mito-Tracker Green is a mitochondria-specific stain for live cells. A 0.2 mM stock solution of Mito-Tracker Green was added to the cell culture medium at a ratio of 1:4000–1:1000, resulting in a final concentration of 50 nM to 200 nM. After treating the cells with the drug, the culture medium was removed and replaced with the prepared Mito-Tracker Green staining solution. The cells were then incubated at 37 °C for 30 min. The labeled cells were imaged using a Leica SP8 confocal microscope.

Synthesis and characterization of B-TTPy

Synthesis of Compound 1. Compound 1 was synthesized according to the previous literature. Di(thiophen-2-yl)methanone (1.06 g, 5.46 mmol), CBr₄ (3.57 g, 10.93 mmol) and PPh₃ (5.73 g, 21.86 mmol) were added in

toluene (25 mL) in flask under nitrogen atmosphere. The mixture was kept at 110 °C for 24 h. After the mixture was cooled to room temperature, water (50 mL) was added. The aqueous layer was extracted three times with dichloromethane, and the organic phase was dried over anhydrous Na_2SO_4. The solvent was then removed under reduced pressure. The residue was purified by silica gel chromatography, using petroleum ether (PE) as eluent to afford Compound 1 as yellow oil (2.03 g, 53.4%). ^{1}H NMR (400 MHz, $CDCl_3$) δ 7.40 (dd, $J = 5.2$, 1.2 Hz, 2H), 7.11 (dd, $J = 3.7$, 1.2 Hz, 2H), 7.01 (dd, $J = 5.1$, 3.7 Hz, 2H).

Synthesis of Compound 2. Compound 1 (0.76 g, 2.17 mmol), pyridine-4-boronic acid (1.07 g, 8.68 mmol), K_2CO_3 (1.12 g, 8.68 mmol) were dissolved in a mixed solution of toluene (40 mL), ethanol (20 mL), and water (2.4 mL) in the flask. Then $Pd(PPh_3)_4$ (0.07 g, 0.06 mmol) was added to the mixture under nitrogen atmosphere. The mixture was kept at 110 °C for 24 h. After the reaction completed, the mixture was cooled to room temperature, water (50 mL) was added. The aqueous layer was extracted three times with dichloromethane, and the organic phase was dried over anhydrous Na_2SO_4. The solvents were then removed under reduced pressure. The solution was purified by silica gel chromatography, using methanol/dichloromethane (1:100, v/v) as eluent to afford compound 2 as yellow solid (0.36 g, 48.0%). ^{1}H NMR (400 MHz, $CDCl_3$) δ 8.47 −8.43 (m, 4H), 7.27 (dd, $J = 5.1$, 1.3 Hz, 2H), 7.03 − 7.00 (m, 4H), 6.84 (dd, $J = 5.1$, 3.6 Hz, 2H), 6.80 (dd, $J = 3.6$, 1.2 Hz, 2H). ^{13}C NMR (101 MHz, $CDCl_3$) δ 150.73, 149.95, 143.57, 135.86, 130.94, 128.04, 126.75, 125.24, 121.42. HRMS (ESI) m/z calcd for $C_{20}H_{15}N_2S_2^+$ [M + H]$^+$ 347.0598, found 347.0670.

Synthesis of Compound 3. Compound 2 (0.05 g, 0.15 mmol), p-toluenesulfonic acid monohydrate (TsOH.H_2O) (0.06 g, 0.32 mmol) were added in ethanol (5 mL) in flask. The mixture was kept at room temperature and stirred 15 min. Then N-Iodosuccinimide (0.07 mg, 0.32 mmol) was added to the reaction mixture, and the mixture was stirred for another 10 min. Afterward, the reaction mixture was stirred at 80 °C for 5 h. After the reaction completed, the solvent was removed. The residue was purified by silica gel chromatography and using methanol/ dichloromethane (1:100, v/v) as eluent to afford compound 3 as yellow solid (0.04 g, 44.4%). ^{1}H NMR (400 MHz, CDCl3) δ 8.51 −8.47 (m, 4H), 7.02 − 6.97 (m, 6H), 6.47 (d, $J = 3.8$ Hz, 2H). ^{13}C NMR (101 MHz, $CDCl_3$) δ 150.17, 149.08, 148.75, 136.79, 132.48, 131.10, 128.31, 126.88, 124.98. HRMS (ESI) m/z calcd for $C_{20}H_{13}I_2N_2S_2^+$ [M + H]$^+$ 598.8531, found 598.8600.

Synthesis of Compound 4. compound 3 (0.12 g, 0.20 mmol), 4-(diphenylamino)phenylboronicacid (0.35 g, 1.20 mmol), K_2CO_3 (0.17 g, 1.20 mmol) in a mixed solution of toluene (40 mL), ethanol (20 mL), and water (2.4 mL) in the flask. Then $Pd(PPh_3)_4$ (0.14 g, 0.12 mmol) was added to the mixture under nitrogen atmosphere. The mixture was kept at 110 °C for 24 h. After the reaction completed, the mixture was cooled to room temperature, water (50 mL) was added. The aqueous layer was extracted three times with dichloromethane, and organic phase was dried over anhydrous Na_2SO_4. The solution was purified by silica gel chromatography, using methanol/dichloromethane (1:200, v/v) as eluent to afford compound 4 as tangerine solid (0.02 g, 12.7%). ^{1}H NMR (400 MHz, DMSO-d6) δ 8.47 (d, $J = 5.1$ Hz, 4H), 7.45 (d, $J = 8.4$ Hz, 4H), 7.32 (t, $J = 7.7$ Hz, 8H), 7.22 (d, $J = 3.9$ Hz, 2H), 7.14 (d, $J = 5.5$ Hz, 4H), 7.06 (dd, $J = 21.9$, 7.6 Hz, 12H), 6.92 (d, $J = 8.5$ Hz, 4H), 6.83 (d, $J = 3.8$ Hz, 2H). ^{13}C NMR (101 MHz, $CDCl_3$) δ 150.14, 149.96, 147.78, 147.32, 146.98, 141.71, 134.79, 132.51, 131.35, 129.36, 127.49, 126.48, 125.43, 124.63, 123.40, 123.30, 121.79. HRMS (ESI) m/z calcd for $C_{56}H_{41}N_4S_2^+$ [M + H]$^+$ 833.2767, found 833.2769.

Synthesis of B-TTPy. Compound 4 (0.08 g, 0.10 mmol) was dissolved in acetonitrile (10 mL) in flask. Then iodomethane (0.91 g, 6.40 mmol) was added. The reaction mixture was stirred at 80 °C for 8 h. After the reaction completed, the mixture was cooled to room temperature. The solvents were then removed under reduced pressure. The resulting crude product was washed with ether and then dried to obtain pure B-TTPy as purple-black solid (0.05 g, 46.4%). ^{1}H NMR (400 MHz, DMSO-d6) δ 8.83 (d, $J = 6.5$ Hz, 4H), 7.80 (d, $J = 7.0$ Hz, 4H), 7.55 (d, $J = 8.7$ Hz, 4H), 7.39 − 7.32 (m, 10H), 7.16 −7.09 (m, 6H), 7.06 (d, $J = 7.1$ Hz, 8H), 6.93 (d, $J = 8.7$ Hz, 4H), 4.27 (s, 6H). ^{13}C NMR (101 MHz, $CDCl_3$) δ 52.48, 146.97, 145.24, 130.41, 129.49, 127.03, 126.07, 125.04, 123.78, 122.60, 49.04. HRMS (ESI) m/z calcd for $C_{58}H_{46}N_4S_2^{2+}$ [M]$^{2+}$ 431.1577, found 431.1575.

All structures and purity of the intermediates and B-TTPy were confirmed by nuclear magnetic resonance spectroscopy (NMR) and high-resolution mass spectrometry (HRMS) (Figs. S1-S13).

Mass spectrometry analysis was performed for structural validation of synthesized compounds. Four samples (no technical replicate, $n = 1$ per compound) were dissolved in HPLC-grade methanol without controls included. Analyses used direct infusion on a High-resolution Ion Mobility LC-MS (AB SCIEX Triple TOF 5600 +) with ESI source (spray voltage: 3.80 kV; capillary temperature: 350 °C; sheath gas flow: 35 arb). Full MS scans (100–1500 m/z) were acquired in positive ion mode at 70,000 resolutions (AGC target: 1×10^6 ions). Data collection used Thermo TraceFinder, with structural validation and spectral processing performed in Thermo Xcalibur Qual Browser via exact mass matching (Δm/z < 1.0 ppm).

Preparation of the engineered cell membrane expressing anti-CD133-scFv

A lentiviral plasmid was designed by combining the green fluorescent protein (GFP) and the farnesyl signal peptide gene with the anti-CD133-scFv gene to monitor expression and target the cell membrane. The sequence of scFv targeting CD133 antigen was derived from AC133 or clone 7[7,40]. The plasmid was then transfected into cells with an encapsulating plasmid to construct the lentivirus. This lentivirus was further transfected into a human megakaryocytic cell line (MEG01) to obtain anti-CD133-scFv +MEG01 cells that stably expressed anti-CD133-scFv on the cell membrane. anti-CD133-scFv +MEG01 cells were pretreated with PMA for 24 h and then induced with a combination of TPO and GSNO for 24 h to promote maturation. After maturation, the cells were collected and resuspended in ACK lysis buffer. Following 1 min of lysis, the reaction was terminated with 10 mL of PBS, and MEG01 cells were collected by centrifugation at 300 × g and 4 °C for 5 min. The cell precipitate was resuspended in 10 mL of PBS buffer and sonicated at 35% power for 5 min using a probe sonicator to disrupt the cells. The suspension was centrifuged at 3000 × g for 5 min and then at 10,000 × g for 10 min at 4 °C, collecting the supernatant and discarding the precipitate each time. Finally, the collected supernatant was centrifuged at 100,000 × g and 4 °C for 2 h, the supernatant was discarded, and the membrane precipitate was collected.

Western blot analysis

Harvested cells were lysed at a ratio of 100:1 (v/v) using RIPA lysis buffer and PMSF protease inhibitor. The protein concentration was determined using the BCA protein assay kit. Equal amounts of protein extracts (20 μg) were separated by 10% SDS–PAGE and transferred to PVDF membranes (Merck Millipore, Billerica, MA, USA). Blocking was performed with skim milk for 1 h at room temperature, followed by overnight incubation at 4 °C with the primary antibody. The membranes were then incubated for 1 h at room temperature with a horseradish peroxidase-conjugated secondary antibody diluted in antibody dilution buffer. Finally, proteins on the membrane were visualized by chemiluminescence (Bio-Rad, Hercules, CA, USA) according to the manufacturer's instructions.

Cell viability

Cells were seeded into 96-well plates at a density of 2×10^3 cells/well and incubated in a CO_2 incubator at 37 °C for 24 h. Afterward, the cells were treated with different drugs for specific time intervals. Next, CCK-8 solution (10 μL) was added to each well for 1 h of incubation. The

absorbance of each well was measured at 450 nm using a microplate reader (Bio-Rad, CA, USA)

Live/dead staining

As previously reported[41], the live/dead viability/cytotoxicity kit was used to assess cell viability parameters following the manufacturer's protocol. Briefly, a staining solution containing calcein-AM and ethidium homodimer-1 was prepared at an appropriate concentration in PBS. The staining solution was mixed with the cell culture medium at a ratio of 1:2 (v/v) and incubated with cells at 37 °C for 30 min. Finally, the labeled cells were visualized using a Leica SP8 confocal microscope (Leica Microsystems).

Cellular localization assay

QL01#GBM cells were seeded in 8-well chambers with 5×10^4 cells per well for confocal microscopy. After 12 h of culture, the cells were incubated with 10 µM B-TTPy for 30 min. The treated cells were observed immediately under a confocal microscope. For the colocalization studies, the cells were incubated with Mito-Tracker Green (10 µM) for 30 min. The cells were viewed immediately under a confocal microscope.

RT-PCR

Reverse transcription reaction was performed in a thermocycler (The LightCycler® 480 II; Roche) using ColorGPS qPCR SYBR Green Master Mix (YEASEN) according to the manufacturer's protocol, under the following conditions: incubation at 25 °C for 5 min, reverse transcription at 42 °C for 30 min, inactivation at 85 °C for 5 min. Real-time PCR (RT-PCR) was carried out in a LightCycler® 480 Software (Roche). The PCR protocol consisted of 40 cycles of denaturation at 95 °C for 30 s and annealing/extension at 60 °C for 30 s. For quantification analysis, the comparative Threshold Cycle (Ct) method was used. The Ct values from each gene were normalized to the Ct value of GAPDH in the same RNA samples. Relative quantification was performed using the 2ΔDDCt method and expressed as fold change in arbitrary values.

Flow cytometry analysis

Mice from each group were euthanized on Day 21 posttreatment. Tumor tissue was collected and ground in a glass grinder by using cold PBS to obtain cell suspension. The suspension was centrifuged at 3000 rpm for 5 min at 4 °C, and the supernatant was discarded. The cells were resuspended in PBS, filtered through a 70 µm nylon cell filter, and counted for flow cytometry analysis. To prevent nonspecific antibody binding, CD16/CD32 (1:1500 dilution) was added to block the cells for 15 min. Anti-CD3-PerCP-Cy5.5 (1:20 dilution), anti-CD4-FITC (1:300 dilution), and anti-CD8-PE (1:200 dilution) were added to stain the cells for $CD3^+CD4^+$ and $CD3^+CD8^+$ T-cell analysis.

Transcriptomic data analysis

Transcriptome and survival data were obtained from the TCGA and GTEx database. Single-cell transcriptome data were sourced from the GEO database (GEO: GSE223065). The Seurat package was employed (version 5.1.0) in R (version 4.4.0) to conduct dimensionality reduction and clustering analysis on the single-cell transcriptomic data. Cells with a high mitochondrial gene expression ratio (>20%) were excluded from our analysis. After standardizing the data using default parameters, the top 2000 highly variable genes were selected and the first 30 principal components for downstream analysis. Subsequently, batch effects between different samples were mitigated using the Harmony method. Visualization was performed using t-distributed Stochastic Neighbor Embedding (t-SNE) with a resolution of 0.2. Finally, after acquiring the expression features of cell clusters via the FindAllMarkers function, cell annotation was carried out.

Dual luciferase reporter assay

Luciferase activities were measured using the Dual Luciferase Reporter Assay system. Briefly, expression plasmids including a firefly luciferase reporter construct, a Renilla luciferase reporter construct, as well as other expression constructs, were transfected into QL01#GBM cells. 24 h post transfection, cells were collected and lysed. The relative luciferase activity was expressed as arbitrary units by normalizing firefly luciferase activity under Ifnb1 promoter to Renilla luciferase activity from a control plasmid.

Theoretical calculations

The geometry of B-TTPy was optimized by DFT calculations using the dispersion corrected M062X functional with the def2-SVP basis set. The vertical excitation were computed by TD-DFT/M062X/def2-SVP calculations. Vibrational frequency calculation for optimized geometry was carried out and zero imaginary frequency was observed. All the theoretical calculations mentioned above were performed using the Gaussian 09 program. The spin-orbit coupling matrix elements (SOCME) were calculated at the TD-DFT/M062X/def2-TZVP level of theory with spin-orbit mean-field (SOMF) methods employing the ORCA 5.0.3 program. The Cartesian coordinates, energies and relative energies are listed in the Source Data file.

Statistics and reproducibility

All data were analyzed using GraphPad Prism 8 software and are presented as the mean ± standard deviation (S.D.). Two-way analysis of variance (ANOVA), the log-rank test, and unpaired two-tailed t tests were used to calculate P values for different experimental purposes. The data were evaluated for normality and equal variance using the t test and were found to be normally distributed. The methods for data collection and analysis were predetermined before the start of the experiments. Unless otherwise specified, all experiments were repeated at least three times. Furthermore, two-sided tests were used for all analyses. Significant differences are indicated as $*P < 0.05$, $**P < 0.01$, $***P < 0.001$, and $****P < 0.0001$.

Reporting summary

Further information on research design is available in the Nature Portfolio Reporting Summary linked to this article.

Data availability

Raw MS/NMR data underlying Figs. S1-S13 are accessible at figshare: https://doi.org/10.6084/m9.figshare.29483873. Single-cell transcriptomic data were sourced from the GEO database (https://www.ncbi.nlm.nih.gov/geo/query/acc.cgi?acc=GSE223065) with accession code of GSE223065. All other data supporting the findings of this study are available in the article, Supplementary Information or Source Data file. Source data are provided with this paper Source data are provided with this paper.

References

1. Herrlinger, U. et al. Lomustine-temozolomide combination therapy versus standard temozolomide therapy in patients with newly diagnosed glioblastoma with methylated MGMT promoter (CeTeG/NOA-09): a randomised, open-label, phase 3 trial. *Lancet* **393**, 678–688 (2019).
2. Stupp, R. et al. Effect of tumor-treating fields plus maintenance temozolomide vs maintenance temozolomide alone on survival in patients with glioblastoma: a randomized clinical trial. *Jama* **318**, 2306–2316 (2017).
3. Malmström, A. et al. Temozolomide versus standard 6-week radiotherapy versus hypofractionated radiotherapy in patients older than 60 years with glioblastoma: the Nordic randomised, phase 3 trial. *Lancet Oncol.* **13**, 916–926 (2012).

4. Hilf, N. et al. Actively personalized vaccination trial for newly diagnosed glioblastoma. *Nature* **565**, 240–245 (2019).

5. Broekman, M. L. et al. Multidimensional communication in the microenvirons of glioblastoma. *Nat. Rev. Neurol.* **14**, 482–495 (2018).

6. Natarajan, S. K. & Venneti, S. Glioblastoma stem cell HISTArionics. *Cell Stem Cell* **29**, 1509–1510 (2022).

7. Chen, C. et al. Intracavity generation of glioma stem cell-specific CAR macrophages primes locoregional immunity for postoperative glioblastoma therapy. *Sci. Transl. Med.* **14**, eabn1128 (2022).

8. Yang, F. et al. Small-molecule toosendanin reverses macrophage-mediated immunosuppression to overcome glioblastoma resistance to immunotherapy. *Sci. Transl. Med.* **15**, eabq3558 (2023).

9. Zheng, X. X. et al. Mitochondria in cancer stem cells: Achilles heel or hard armor. *Trends Cell Biol.* **33**, 708–727 (2023).

10. Viale, A. et al. Oncogene ablation-resistant pancreatic cancer cells depend on mitochondrial function. *Nature* **514**, 628–632 (2014).

11. Mangalhara, K. C. et al. Manipulating mitochondrial electron flow enhances tumor immunogenicity. *Science* **381**, 1316–1323 (2023).

12. Zhang, Y. et al. Blood–brain barrier penetrating nanovehicles for interfering with mitochondrial electron flow in glioblastoma. *ACS Nano* **18**, 9511–9524 (2024).

13. He, B. et al. Cancer cell employs a microenvironmental neural signal trans-activating nucleus-mitochondria coordination to acquire stemness. *Signal Transduct. Target. Ther.* **8**, 275 (2023).

14. Molina, J. R. et al. An inhibitor of oxidative phosphorylation exploits cancer vulnerability. *Nat. Med.* **24**, 1036–1046 (2018).

15. Chakrabarty, R. P. & Chandel, N. S. Mitochondria as signaling organelles control mammalian stem cell fate. *Cell Stem Cell* **28**, 394–408 (2021).

16. Zhang, J. et al. Systematic identification of anticancer drug targets reveals a nucleus-to-mitochondria ROS-sensing pathway. *Cell* **186**, 2361–2379.e2325 (2023).

17. Gulen, M. F. et al. cGAS-STING drives ageing-related inflammation and neurodegeneration. *Nature* **620**, 374–380 (2023).

18. Lim, M., Xia, Y., Bettegowda, C. & Weller, M. Current state of immunotherapy for glioblastoma. *Nat. Rev. Clin. Oncol.* **15**, 422–442 (2018).

19. Jackson, C. M., Choi, J. & Lim, M. Mechanisms of immunotherapy resistance: lessons from glioblastoma. *Nat. Immunol.* **20**, 1100–1109 (2019).

20. Kroemer, G. & Pouyssegur, J. Tumor cell metabolism: cancer's Achilles' heel. *Cancer cell* **13**, 472–482 (2008).

21. Gaharwar, A. K., Singh, I. & Khademhosseini, A. Engineered biomaterials for in situ tissue regeneration. *Nat. Rev. Mater.* **5**, 686–705 (2020).

22. Han, C., Kundu, B. K., Liang, Y. & Sun, Y. Near-infrared light-driven photocatalysis with an emphasis on two-photon excitation: concepts, materials, and applications. *Adv. Mater.* **36**, e2307759 (2024).

23. Feng, C. et al. Light-activated chemical probing of nucleobase solvent accessibility inside cells. *Nat. Chem. Biol.* **14**, 276–283 (2018).

24. Kokel, D. et al. Photochemical activation of TRPA1 channels in neurons and animals. *Nat. Chem. Biol.* **9**, 257–263 (2013).

25. Liu, Y. et al. Highly twisted conformation thiopyrylium photosensitizers for in vivo near infrared-II imaging and rapid inactivation of coronavirus. *Angew. Chem.* **62**, e202214875 (2023).

26. Ward, N. P. Cys-regulation: oxidized CHK1 controls cross-compartment circuit of chemoresistance. *Trends Cancer* **9**, 700–702 (2023).

27. Paquet, N. et al. hSSB1 (NABP2/ OBFC2B) is required for the repair of 8-oxo-guanine by the hOGG1-mediated base excision repair pathway. *Nucleic Acids Res.* **43**, 8817–8829 (2015).

28. Tan, K. et al. Mitochondrial SSBP1 protects cells from proteotoxic stresses by potentiating stress-induced HSF1 transcriptional activity. *Nat. Commun.* **6**, 6580 (2015).

29. Graham A. J. et al. Transcriptional regulation of living materials via extracellular electron transfer. *Nat. Chem. Biol.* **20**, 1329-1340 (2024).

30. Zhang Y. et al. Implantable microneedle-mediated eradication of postoperative tumor foci mitigates glioblastoma relapse. n/a, 2409857.

31. Jiao K. et al. Bioprinting extracellular vesicles as a "cell-free" regenerative medicine approach. *Extracell. Vesicles Circ. Nucl. Acids.* **4**, 218-239 (2023).

32. Zhang, Y. et al. Stimulation of tumoricidal immunity via bacteriotherapy inhibits glioblastoma relapse. *Nat. Commun.* **15**, 4241 (2024).

33. Omuro, A. & DeAngelis, L. M. Glioblastoma and other malignant gliomas: a clinical review. *Jama* **310**, 1842–1850 (2013).

34. Gimple, R. C., Yang, K., Halbert, M. E., Agnihotri, S. & Rich, J. N. Brain cancer stem cells: resilience through adaptive plasticity and hierarchical heterogeneity. *Nat. Rev. Cancer* **22**, 497–514 (2022).

35. Wang, Q. et al. Tumor evolution of glioma-intrinsic gene expression subtypes associates with immunological changes in the microenvironment. *Cancer cell* **32**, 42–56.e46 (2017).

36. DeBerardinis, R. J. & Chandel, N. S. Fundamentals of cancer metabolism. *Sci. Adv.* **2**, e1600200 (2016).

37. Kroemer, G., Galassi, C., Zitvogel, L. & Galluzzi, L. Immunogenic cell stress and death. *Nat. Immunol.* **23**, 487–500 (2022).

38. Jiang, M. et al. cGAS-STING, an important pathway in cancer immunotherapy. *J. Hematol. Oncol.* **13**, 81 (2020).

39. Li, A. et al. Activating cGAS-STING pathway for the optimal effect of cancer immunotherapy. *J. Hematol. Oncol.* **12**, 35 (2019).

40. Vora, P. et al. The rational development of CD133-targeting immunotherapies for glioblastoma. *Cell Stem Cell* **26**, 832–844.e836 (2020).

41. Zhang, Y. et al. Glioblastoma therapy using codelivery of cisplatin and glutathione peroxidase targeting siRNA from iron oxide nanoparticles. *ACS Appl. Mater. Interfaces* **12**, 43408–43421 (2020).

Acknowledgements

Author contributions

L.L.C. designed the project, synthesized and characterized the samples. Z.Z.F. and J.P.W. carried out the in vitro/vivo experiments. K.Y.X., Y.Z., F.F. took part in the discussion and gave important suggestions. L.Y. carried out theoretical calculations. M.S. and J.J.W. interpreted the results. Z.M.W., K.N.W., and T.D. drafted/revised the manuscript. S.L.N., Y.R.Z. and Y.L.Z. designed and advised the project.

Competing interests

The authors declare no competing interests.

Additional information

[1]College of Chemistry & Pharmacy, Northwest A&F University, Shaanxi Yangling, PR China. [2]Department of Neurosurgery, Shandong Key Laboratory of Brain Health and Function Remodeling, Qilu Hospital of Shandong University, Cheeloo College of Medicine, Shandong University, Jinan, Shandong, PR China. [3]Key Laboratory of Synthetic and Natural Functional Molecule of the Ministry of Education, College of Chemistry & Materials Science, Northwest University, Xi'an, Shaanxi, PR China. [4]Department of Biochemistry, Faculty of Pharmacy, University of Santo Tomas, Manila, Philippines. [5]Faculty of Medicine and Health Sciences, School of Pharmacy, University of Auckland, Auckland, New Zealand. [6]State Key Laboratory of Crystal Materials, Shandong University, Jinan, Shandong, PR China. [7]University of Bordeaux, CNRS, Bordeaux, France. [8]Jinan Microecological Biomedicine Shandong Laboratory, Jinan, Shandong, PR China. [9]These authors contributed equally: Lulu Cheng, Zezheng Fang, Junpeng Wang. ✉e-mail: nishilei@sdu.edu.cn; zhangyr@nwsuaf.edu.cn; Yulin.Zhang@sdu.edu.cn